J. of Supercritical Fluids 50 (2009) 193–202

Contents lists available at ScienceDirect

The Journal of Supercritical Fluids

journal homepage: www.elsevier.com/locate/supflu

High-pressure phase equilibria of systems carbon dioxide + *n*-eicosane and propane + *n*-eicosane

S.B. Rodriguez-Reartes [a], M. Cismondi [b], E. Franceschi [c], M.L. Corazza [c,1], J. Vladimir Oliveira [c], M.S. Zabaloy [a,*]

[a] *Planta Piloto de Ingeniería Química - Universidad Nacional del Sur - CONICET - CC 717 - 8000 Bahía Blanca, Argentina*
[b] *Facultad de Ciencias Exactas Físicas y Naturales, Universidad Nacional de Córdoba, Av. Vélez Sarsfield 1611, Ciudad Universitaria, X5016GCA Córdoba, Argentina*
[c] *Laboratório de Temodinâmica Aplicada – URI-Campus de Erechim, Av. Sete de Setembro 1621, Erechim, RS, Brazil*

ARTICLE INFO

Article history:
Received 26 February 2009
Received in revised form 16 June 2009
Accepted 23 June 2009

Keywords:
Solid–fluid equilibrium
Fluid–fluid equilibrium
n-Eicosane
Propane
Carbon dioxide
Experimental
Theoretical methods

ABSTRACT

In this work we investigated the phase equilibrium behavior of the binary asymmetric systems propane (C3) + *n*-eicosane (C20) and carbon dioxide (CO_2) + *n*-eicosane (C20). We used a variable-volume view cell for obtaining fluid–fluid equilibrium (FFE), solid–fluid equilibrium (SFE) and solid–fluid–fluid equilibrium (SFFE) experimental data. We modeled the phase equilibria of both systems using the Peng–Robinson Equation of State for describing the fluid phases and an expression for the fugacity of pure solid *n*-eicosane with parameters fit to reproduce the pure *n*-eicosane melting line. We performed the phase equilibrium calculations by implementing path-following methods for tracking entire solid–fluid (SF) and solid–fluid–fluid (SFF) equilibrium curves for binary asymmetric mixtures. This made it possible to obtain complete isoplethic lines or complete three-phase equilibrium lines in single runs. Although the model is relatively simple, it is able to grasp the complex observed behavior for the systems studied here.

1. Introduction

Several phase equilibrium studies of binary asymmetric mixtures involving a long-chain *n*-paraffin and a volatile compound have been previously carried out [1]. These mixtures are of special interest due to their potential for formation of solid deposits. Their study provides insight about a number of problems of practical interest, such as the undesired appearance of solid deposits composed of long-chain molecules during exploitation, production and transport of petroleum fluids, or while using diesel or biodiesel fuels in vehicles. Binary asymmetric mixtures present a quite complex phase behavior [2,3]. This makes the modeling (and even the calculation) of the fluid–fluid and solid–fluid phase behavior, in wide ranges of conditions, a challenging task.

In this work, we report new phase equilibrium experimental data for the systems carbon dioxide + *n*-eicosane and propane + *n*-eicosane. The ranges of conditions correspond to equilibria involving both, fluid and solid phases.

The propane + *n*-eicosane system exhibits type I or II phase behavior [4] according to the classification of fluid phase behavior of Scott and van Konynemburg [5]. Thus, the vapor–liquid critical line extends from the critical point of pure propane to the critical point of pure *n*-eicosane. No three-phase LLV equilibrium line has been observed for this system [4,6], i.e., *n*-eicosane is completely miscible with propane in the liquid phase. A solid–liquid–vapor (SLV) equilibrium line extending from the pure C20 triple point to lower temperatures is expected for this system [4].

To our knowledge, no experimental information has been reported on SL phase boundaries, or on the SLV locus, for the system propane + *n*-eicosane. One of the purposes of the present work is to fill this gap.

Carbon dioxide + *n*-alkane binary mixtures show partial miscibility in liquid phase [7]. For carbon dioxide + *n*-eicosane mixtures, type III E diagrams are expected according to Luks [7]. Type III E diagrams are as type III global phase equilibrium diagrams of the Scott and van Konynemburg classification [5], but with a LLV equilibrium line interrupted by a quadruple (Q) point, where a solid phase appears. At the Q point, three other three-phase equilibrium lines meet, i.e., two SLV curves and a SLL line. This work involves the experimental determination of LL, SL, LLV and SLL equilibria for the carbon dioxide + *n*-eicosane system. Even though Huie et al. [8] have already obtained LV, LLV and SLV experimental data for the system CO_2 + C20, and other authors [9–13] have also measured fluid–fluid

* Corresponding author. Tel.: +54 291 486 1700x232; fax: +54 291 486 1600.
E-mail address: mzabaloy@plapiqui.edu.ar (M.S. Zabaloy).
[1] Present address: Setor de Tecnologia, Departamento de Engenharia Química, Universidade Federal do Paraná, Caixa Postal 19011, Centro Politécnico, Jardim das Américas, Curitiba, PR, Brasil.

0896-8446/$ – see front matter © 2009 Elsevier B.V. All rights reserved.
doi:10.1016/j.supflu.2009.06.017

transitions for this system, neither SL nor SLL phase boundaries have, to our knowledge, been reported, for CO_2 + C20, until now, in the present work.

In this work, we propose a modeling approach for the solid–fluid equilibria which, among other features, pays close attention to the reproduction of the solid–liquid (melting) line of the pure heavy component (C20) in a wide pressure range. Since we have chosen to describe the properties of the fluid phases using the Peng–Robinson Equation of State, it is clear that we study in the present work one of the simplest forms of a general modeling approach. Once we have chosen a model, the further calculation of fluid–fluid–solid or fluid–solid equilibrium lines may be difficult. We tackle such problem by using numerical continuation methods (see, e.g., Ref. [14]). They are robust and fast.

2. Experimental

2.1. Materials

Carbon dioxide (99.9 wt% in the liquid phase) and propane (99.5 wt% in the liquid phase, denominated 2.5) were purchased from White Martins S.A. and *n*-eicosane (99 wt%) was purchased from Sigma–Aldrich. We used all these materials without further purification.

2.2. Apparatus and experimental procedure

Phase equilibrium experiments were carried out in a high-pressure variable-volume view cell. The experimental apparatus and procedure have been used in a variety of previous studies [15–17]. Briefly, the experimental device consists of a variable volume view cell with two sapphire windows for visual observation, an absolute pressure transducer (SMART LD 301, accuracy 0.03 MPa), a portable programmer (NOVUS, 521/3D) for the cell pressure data acquisition, and a syringe pump (ISCO 260D). The equilibrium cell has a movable piston, which makes possible to control the pressure inside the cell. The pure solvent was always used as the pressure transmission fluid. A metallic jacket surrounds the cell. Water from a thermostatic bath is used as heating/cooling fluid, which flows through the jacket, so that the cell is kept at the desired temperature. The temperature of the mixture inside the cell is measured within 0.1 K using a type "Y" thermocouple.

Phase transitions were achieved by manipulating the pressure (fluid–fluid transitions) or through temperature changes [solid–fluid or solid–(fluid–fluid) transitions]. Pressure changes were imposed by using the syringe pump. Temperature changes were carried out through set point changes in the thermostatic bath.

The experimental procedure is as follows: [i] an amount of the heavy component is accurately weighed on a precision scale balance (SHIMADZU AY220 with 0.0001 g accuracy) and loaded into the equilibrium cell. [ii] Then, a known amount of the light component (propane or carbon dioxide) is introduced into the cell with the help of a syringe pump so that the desired overall composition is obtained. From the estimated uncertainties in the quantities of the loaded gas and solute (*n*-eicosane), it was possible to estimate, through propagation of error analysis (see Appendix A), that the maximum uncertainties in mole fraction values here reported were never greater than 0.7%, 1.7% and 0.11% for *n*-eicosane, propane and carbon dioxide respectively (the average uncertainties were less than 0.62%, 0.4% and 0.03%, respectively). The corresponding maximum uncertainties for the overall weight fractions were about 0.7%, 2.2% and 0.4% for *n*-eicosane, propane and carbon dioxide respectively (the average uncertainties were less than 0.6%, 0.6% and 0.1%, respectively). For computing these maximum uncertainty levels, we considered all overall concentration values reported in this work. [iii] Once the cell was loaded with a mixture at the desired overall composition, the content was kept at continuous agitation helped by a magnetic stirrer and a Teflon-coated stirring bar. Three different procedures were used depending on the type of phase transitions we wanted to achieve: *(a) Fluid–fluid transitions*: For these kind of measurements the temperature controller was turned on, and, once the desired temperature was reached within 0.1 K, the system pressure was increased until the visualization of a single-phase system in the cell. At this point the system was stabilized for at least 30 min. Then, the pressure was slowly decreased (typically at a rate of 0.1–0.3 MPa/min) until the incipient formation of a new phase was observed. This procedure was repeated at least three times for each set temperature and set global composition, with a reproducibility level of 0.2 bar. After completion of the measurement at a given temperature, the cell temperature was set at a new value and the experimental procedure was repeated. *(b) Solid–fluid transitions*: In this case, the cell pressure was set at a desired value. Then, the cell was heated until the visualization of a single–fluid phase system, and stabilized at these conditions for at least 30 min. Next, the temperature was slowly decreased (generally at a rate of 0.1–0.2 K/min) until the incipient appearance of a solid phase. Then, the system was reheated until completing the re-dissolution of the previously formed solid, thus making possible to carry out a new measurement of the transition, at the same pressure. The experimental procedure was repeated at least three times for each condition, with a reproducibility level of 0.5 K. *(c) Solid–(fluid–fluid) transitions*: For this kind of transition, the procedure was similar to the one described in item (b). The difference was that, when heating the system, a two-phase (fluid–fluid) system was achieved instead of a single–fluid-phase system. By using this procedure, it is possible to measure FF → SFF transitions in a range of pressure values, at a set global composition.

Our procedure for measuring phase transitions involving solids consists of looking for the temperature of appearance of a solid phase, i.e., we search for a freezing point rather than for a melting point. This was also the choice that Cheong et al. [18] made, on the grounds of a lower scattering of the data. Cheong et al. [18] ascribed the lower self-consistency of the melting point data, with respect to that of the freezing point data, to a possible non-uniformity of the fluid phase composition when the solid begins to melt.

The procedure for obtaining liquid–liquid–vapor equilibrium data was similar to procedure (a). The difference was that, after finding a pressure condition such that the system consisted of two fluid phases, the pressure was further decreased up to the observation of the appearance of a third (vapor) phase.

It is important to stress that we used the syringe pump not only to load the light component into the cell, but also to automatically control the rate of change of the system pressure, when looking for the appearance of a new fluid phase.

Considering the experimental procedures previously described, we estimated the uncertainty in the temperature values here reported to be less than 0.5 K, and the uncertainty in the reported pressure values to be less than 1 bar.

2.3. Experimental results

Table 1 presents experimental liquid–liquid–vapor (LLV) equilibrium data for the CO_2 + *n*-eicosane system obtained in this work. The (T, P) coordinates of Table 1 data appear plotted in Fig. 1 together with the LLV data of Huie el al. [8] and of Fall et al. [19]. Fig. 1 shows that our LLV experimental results are consistent with previous data.

Table 2 presents the experimental liquid–liquid (LL) and solid–liquid (SL) equilibrium data for the system CO_2 + *n*-eicosane that we obtained in this work. Table 3 reports our experimental solid–liquid–liquid (SLL) equilibrium data for the same binary system. The data in Tables 2 and 3 are plotted in Fig. 2, which

Table 1
Experimental liquid–liquid–vapor (LLV) equilibrium data for the system CO_2 + *n*-eicosane (this work).

LL → LLV transitions		
Overall *n*-eicosane mole fraction[a] in equilibrium cell	*T* (K)	*P* (bar)
0.135645	302.85	69.7
0.135645	300.85	67.4
0.008146	303.15	71.0
0.004777	302.85	72.45
0.004777	303.75	74.2
0.004777	305.25	76.0
0.001571	303.45	71.2

[a] The uncertainties in mole fraction values are reported in Section 2.2.

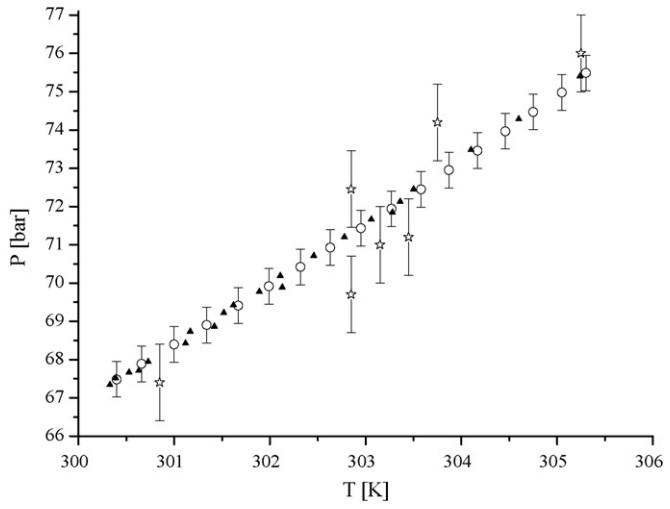

Fig. 1. Experimental liquid–liquid–vapor (LLV) equilibria for the system carbon dioxide + *n*-eicosane: pressure–temperature projection. *Experimental data*: (☆) this work; (○) Huie el al. [8]; (▲) Fall et al. [19]. Error bars for the experimental pressure are also presented on this chart, except for the data from Ref. [19], whose authors estimated a pressure accuracy of ±0.07 bar (not shown here).

shows a good consistency among our LL, SL and SLL experimental data for the system CO_2 + *n*-eicosane. The pressure range of our SLL data is from 71.2 to 250 bar. We obtained such SLL data by the procedure depicted in item (c), starting from a two-phase system (liquid–liquid). The set of SLL measurements were started at the lowest pressure where a two-phase (LL) system was observed without the appearance of a third phase (i.e., a vapor phase). While experimentally exploring the LLV conditions for CO_2 + *n*-eicosane,

Table 2
Experimental liquid–liquid (LL) and solid–liquid (SL) equilibrium data for the system CO_2 + *n*-eicosane (this work).

Liquid phase *n*-eicosane mole fraction[a]	L → LL transitions		L → SL transitions	
	T (K)	*P* (bar)	*T* (K)	*P* (bar)
0.001571	303.35	71.6		
	313.55	95		
	323.85	117		
	333.45	134.6		
0.003142	303.15	83.9	299.85	81.1
	312.45	104.3	299.85	91.1
	322.65	123.6	299.45	101.3
	332.45	147.2		
0.004777	304.35	113.9	301.55	120.6
	314.35	129.8	300.65	130.7
	323.35	148.6	300.55	140.9
	333.15	169.2		

[a] The uncertainties in mole fraction values are reported in Section 2.2.

Table 3
Experimental solid–liquid–liquid (SLL) equilibrium data for the system CO_2 + *n*-eicosane (this work).

LL → SLL transitions		
Overall *n*-eicosane mole fraction[a] in equilibrium cell	*T* (K)	*P* (bar)
0.017023	302.95	250.0
	302.95	220.4
	301.85	150.8
	300.85	102.2
	300.05	71.2

[a] The uncertainties in mole fraction values are reported in Section 2.2.

we observed the appearance of a solid phase at conditions similar to those reported for the quadruple point by Huie et al. [8]. Fig. 7 shows, among other items our SLL and LLV experimental data together with the SLV and quadruple point (Q) experimental data of Huie et al. [8]. Our SLL data are consistent with the Q point reported in the literature [8].

Table 4 presents our raw LV and SL experimental data for the system propane + *n*-eicosane. We obtained this data by searching for a phase transition from a initial condition corresponding to a single liquid phase. Some of Table 4 data appear plotted in Fig. 3, which shows both solid–fluid and fluid–fluid isopleths.

Table 5 presents *PT* coordinates for the solid–liquid–vapor (SLV) equilibrium of the C_3H_8 + *n*-eicosane system estimated by intersecting our LV and SL isopleths. The dashed line in Fig. 3 is the SLV line obtained from smoothing Table 5 data. The shape of such dashed line is consistent with the expectation of a solid–liquid–vapor (SLV) equilibrium line extending from the pure C20 triple point to lower temperatures (see Section 1).

Fig. 4 shows, among other items, all of our experimental solid–fluid equilibrium data together, for the system propane + *n*-eicosane. We have also included in Fig. 4 the pure *n*-eicosane melting data, available in Ref. [20]. From Fig. 4, it is clear that the appearance of solid *n*-eicosane occurs at higher temperature for higher *n*-eicosane concentrations.

3. Modeling

To carry out phase equilibrium computations we need expressions for calculating fugacities of all the system components in all

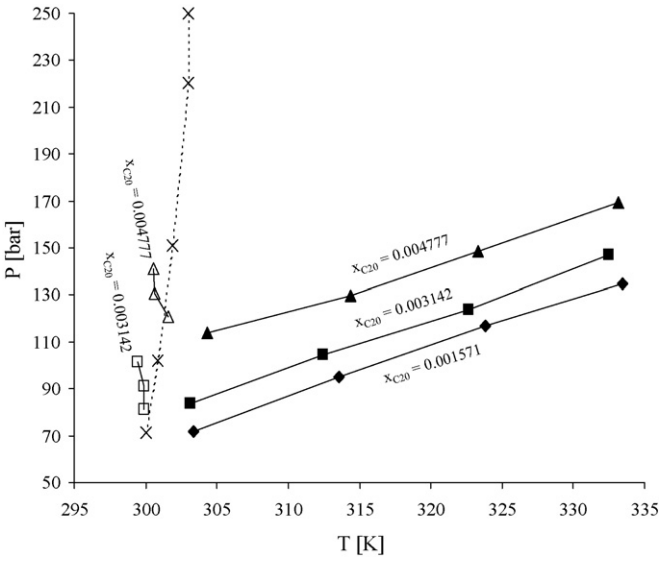

Fig. 2. Pressure–temperature diagram for the system CO_2 + *n*-eicosane. Experimental isoplethic phase equilibrium data (this work). Filled markers: Liquid–liquid; empty markers: solid–liquid; crosses: solid–liquid–liquid.

Table 4
Experimental liquid–vapor (LV) and solid–liquid (SL) equilibrium data for the system C_3H_8 + *n*-eicosane (this work).[a].

Liquid phase *n*-eicosane mole fraction[b]	L → LV transitions		L → SL transitions	
	T (K)	*P* (bar)	*T* (K)	*P* (bar)
0.009816	294.45	9.7		
	298.75	10.6		
	303.95	12.1		
	309.05	13.6		
	313.15	14.9		
	322.55	18		
	332.25	21.9		
0.026720	293.15	9.4		
	303.85	12		
	312.85	14.3		
	322.95	17.7		
	332.15	21.7		
0.113130	288.55	9	287.35	12.2
	298.95	10.6	287.25	15.3
	304.45	12	287.05	20.4
	313.55	14.5		
	323.15	17.4		
	332.45	20.8		
0.134356	293.15	9.2	287.95	12.4
	303.55	11.2	288.35	15.6
	313.35	13.5	288.25	19.2
	323.35	16.6		
	333.45	20.5		
0.159166	293.55	9.9	289.45	12.1
	304.15	12.3	289.55	15.2
	313.45	14.8	289.75	20.3
	322.55	17.5		
	333.15	21.2		
0.222115	295.25	10.1	293.25	12.7
	303.65	12.1	293.25	15.2
	313.55	14.2	293.35	20.3
	323.35	16.8		
	333.35	20.2		
0.354909			298.35	15.4
			298.35	18.4
			298.45	22.5
0.499417	307.15	9	301.75	10.3
	313.55	9.6	301.95	15.3
	323.25	10.9	301.85	20.4
	332.95	12.5		
0.595405	309.85	9.4	304.55	10.4
	319.25	9.9	304.45	15.1
	324.05	10.4	304.45	20.4
	333.25	11.4		
0.747668	314.15	8.4	307.25	11.4
	323.55	8.6	307.15	14.9
	333.15	9	307.15	20.1

[a] All equilibrium data for L → LV transitions are bubble point type.
[b] The uncertainties in mole fraction values are reported in Section 2.2.

Table 5
Estimated solid–liquid–vapor[a] (SLV) equilibrium for the system C_3H_8 + *n*-eicosane.

SLV equilibrium		
Liquid phase *n*-eicosane mole fraction	*T* (K)	*P* (bar)
0.113130	287.48	8.8
0.134356	287.55	8.5
0.159166	289.33	9.1
0.222115	293.19	9.8
0.499417	301.58	8.6
0.595405	304.57	9.2
0.747668	307.3	8.4

[a] Estimated in this work from information in Table 4.

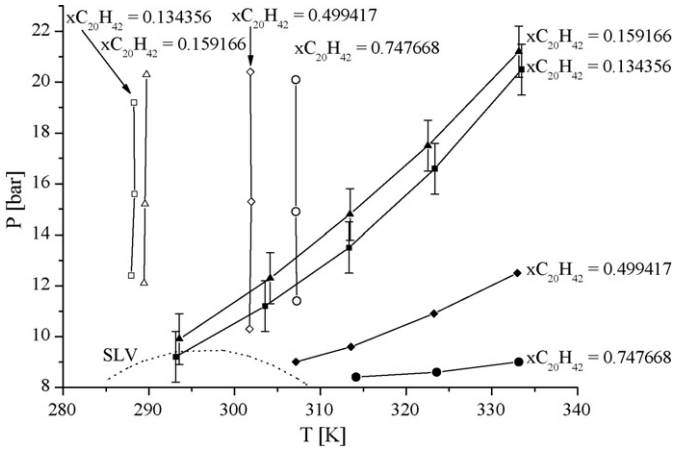

Fig. 3. Experimental solid–fluid (empty markers) and fluid–fluid (bubble points, filled markers) equilibrium isopleths for the propane + *n*-eicosane system (this work). For $xC_{20}H_{42}$ = 0.159166 and $xC_{20}H_{842}$ = 0.134356 we present the pressure experimental error bars. Dashed line: solid–liquid–vapor locus (estimated from smoothing Table 5 data).

equilibrium phases. We use in this work the Peng–Robinson Equation of State (PR-EoS) [21] for calculating component fugacities in fluid mixtures and pure compound fugacities in fluid state.

For the highly asymmetric systems that we consider here, we assume that the solid phase, in any equilibrium situation, is composed of only the pure heavy compound. Thus, once we establish an equation for calculating the fugacity of the pure solid as a function of temperature and pressure, and adopt the PR-EoS for the fluid phases, we can calculate both, solid–fluid and solid–fluid–fluid equilibria. In this work, we use numerical continuation methods for all phase equilibrium computations (see, e.g., Ref. [14]). Continuation methods are known for their ability to track highly curved lines.

The fugacity of the pure heavy component in solid state at system *T* and *P*, i.e., $f_2^S(P, T)$ is given in this work by the following equation:

$$f_2^S(P,T) = [f_2(T,P)]_{pure,liquid} \ \exp(U) \quad (1)$$

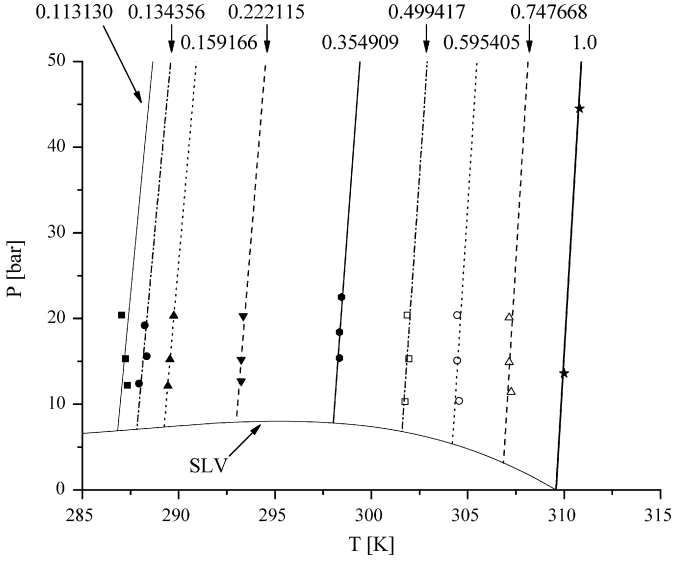

Fig. 4. Solid–fluid equilibrium isopleths for the system propane + *n*-eicosane. The numerical labels correspond to fluid phase *n*-eicosane mole fraction values. Markers: experimental data {this work, except for pure *n*-eicosane (☆) [20]}. Lines: model used with ΔV^{SL} values in Table 9, except for the line labeled as SLV which is the solid–liquid–vapor equilibrium line, calculated with the model using $\Delta V^{SL} = -0.0244054587\ m^3/kmol$, which equals Table 9 C3–C20 average value for ΔV^{SL}.

Table 6
Properties of pure compounds.

Compound	T_{tp} (K)[a]	P_{tp} (Pa)[b]	T_{crit} (K)[a]	P_{crit} (Pa)[a]	ω[a]
Propane			369.83	4,248,000	0.152291
CO_2			304.21	7,383,000	0.223621
n-Eicosane	309.58	2.10470817 10^{-2}	768	1,160,000	0.906878

[a] From DIPPR database [22]. T_{crit}: critical temperature; P_{crit}: critical pressure. ω: acentric factor.

[b] P_{tp}: PR-EoS pure compound vapor–liquid equilibrium pressure at the triple point temperature T_{tp} (this work).

We calculate $[f_2(T,P)]_{pure,liquid}$, i.e., the fugacity of the pure heavy component in (hypothetical) liquid state at system T and P, using the PR-EoS. The variable U is defined as follows:

$$U = \frac{\Delta V^{SL}}{RT_{tp}}\left[C_1\left(1-\frac{T_{tp}}{T}\right)+C_2\left(\frac{T_{tp}}{T}-1+\ln\left(\frac{T}{T_{tp}}\right)\right)+C_3\left(\frac{T}{2T_{tp}}-1+\frac{T_{tp}}{2T}\right)+\frac{T_{tp}}{T}(P-P_{tp})\right] \quad (2)$$

In Eq. (2), the constants T_{tp}, P_{tp} (see Table 6), ΔV^{SL}, C_1, C_2 and C_3 correspond to the pure heavy component (component 2, i.e., *n*-eicosane). ΔV^{SL} is the solid–liquid molar volume difference ($\upsilon_{solid} - \upsilon_{liquid}$) for pure *n*-eicosane. Constants C_1, C_2 and C_3 characterize the pure heavy component solid–liquid equilibrium curve (melting curve). R is the universal gas constant. We obtained Eq. (2) by extending a derivation available in Ref. [23] to the case of a solid–liquid heat capacity difference set as a linear function of temperature.

We obtained the parameters C_1, C_2 and C_3 for *n*-eicosane by regression of the pure *n*-eicosane solid–fluid equilibrium experimental data from Ref. [20]. Table 8 reports the resulting values for C_1, C_2 and C_3.

The systems of equations for calculating phase equilibria arise from imposing the equality of component fugacities in all phases, as well as the uniformity of temperature and pressure throughout the heterogeneous system.

3.1. Parameterization of the PR-EoS

To describe the fluid phase behavior of the systems studied, first we fitted the PR-EoS [21] interaction parameters k_{ij} (attractive) and l_{ij} (repulsive) by reproducing our experimental fluid–fluid equilibrium data. For the system $C_3H_8 + n\text{-}C_{20}H_{42}$, we fitted our bubble pressure data; and for the system $CO_2 + n\text{-}C_{20}H_{42}$, our fluid–fluid equilibrium data. We used the SPECS [24] software package for fitting the parameters. The properties of the pure substances used in the present work are presented in Table 6. Only T_{crit}, P_{crit} and ω appear in the PR-EoS. Table 7 reports the optimum k_{ij} and l_{ij} values we found.

3.2. Modeling results

By imposing equal fugacities for the pure solid and the pure liquid in Eq. (1), it is possible to obtain an expression for the solid–liquid saturation pressure P as a function of temperature T and of constants C_1, C_2 and C_3. Fig. 5 shows the ability of Eq. (1) (used with Table 8 parameter values) to reproduce the pure *n*-eicosane solid–liquid equilibrium curve, in a wide pressure range, by comparison with experimental melting line data from Ref. [20].

Table 7
Binary interaction parameters for the PR-EoS (this work).

System	k_{ij}	l_{ij}	Source of experimental data
$C_3H_8 + n$-eicosane	0.0485	−0.0386	This work
$CO_2 + n$-eicosane	0.0933	0.0054	This work

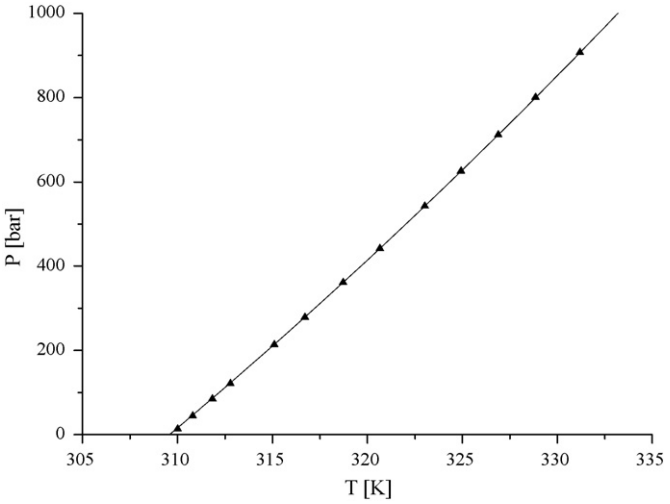

Fig. 5. Solid–liquid equilibrium curve for pure *n*-eicosane. (▲) Experimental melting line data for pure *n*-eicosane [20]. Line: model (this wok).

Table 8
n-Eicosane constants for Eq. (2).

C_1 (bar)	−11,688.9617
C_2 (bar)	34,047.5683
C_3 (bar)	−70,535.1757

The value of ΔV^{SL} does not affect the pure heavy compound melting curve at set values of C_1, C_2 and C_3. Therefore we can use parameter ΔV^{SL} as a degree of freedom to obtain the best possible reproduction of solid–fluid equilibrium data. This is the approach we adopted in this work.

We intended to correlate our solid–fluid experimental data for the $C_3H_8 + n\text{-}C_{20}H_{42}$ system by using a unique value for ΔV^{SL} and found that the model performance was not satisfactory enough. We were able, however, to correlate individual isoplethic data sets. Table 9 reports the resulting ΔV^{SL} values for $C_3H_8 + n\text{-}C_{20}H_{42}$. Fig. 4 shows our calculated and experimental solid–fluid equilibrium isopleths for the system propane + *n*-eicosane. We observe a good level of agreement, which we obtained at the expense of not having a single value for the ΔV^{SL} parameter for this system. Fig. 4 also presents a line labeled as SLV. It is the solid–liquid–vapor equilibrium line, calculated with the model using $\Delta V^{SL} = -0.0244054587\ m^3/kmol$. This is Table 9 average value for ΔV^{SL} of propane + *n*-eicosane. As it was the case for the dashed line of Fig. 3, the shape of Fig. 4 SLV line is consistent with the expectation of a solid–liquid–vapor (SLV) equilibrium line extending from the pure C20 triple point to lower temperatures (see Section 1).

Table 9
ΔV^{SL} values for Eq. (2).

System	Heavy component mole fraction	ΔV^{SL} (m^3/kmol)
$C_3H_8 + n$-eicosane	0.113130	−0.0180999869
	0.134356	−0.0190606549
	0.159166	−0.0204406020
	0.222115	−0.0243716919
	0.354909	−0.0300064985
	0.499417	−0.0344533180
	0.595405	−0.0422779461
	0.747668	−0.0545822546
$CO_2 + n$-eicosane	All	−0.0725476936

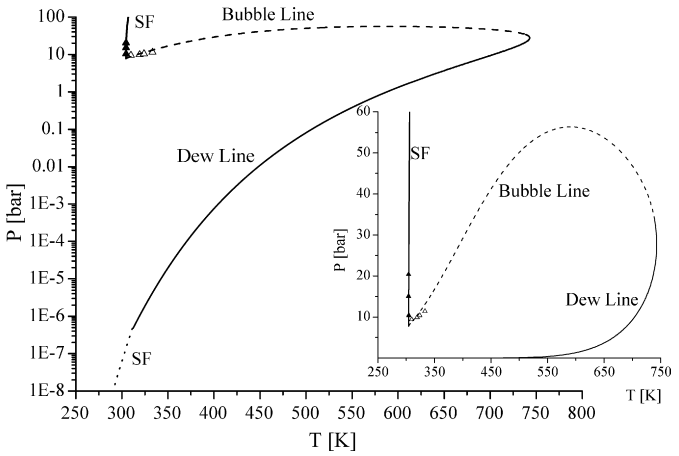

Fig. 6. Isopleth for the system $C_3H_8 + C_{20}H_{42}$ at 0.595405 $C_{20}H_{42}$ fluid phase mole fraction. Filled triangles: experimental solid–fluid equilibrium data (this work). Empty triangles: experimental bubble point data (this work). Lines: model. (- - -) Bubble line; thin solid line: Dew line; thick solid line: solid–liquid equilibrium; (···) solid–vapor equilibrium.

Fig. 6 shows the isopleth at 0.595405 $C_{20}H_{42}$ mole fraction in the fluid phase for the system $C_3H_8 + C_{20}H_{42}$. The lines correspond to the model and the markers to our experimental data. The model gives a phase envelope made of a low-pressure solid–vapor segment, followed by a dew point segment, a bubble point segment and a solid–liquid line. We observe a good agreement with our experimental data. Notice that the solid–vapor segment is visible because of the log scale for pressure. The inset in Fig. 6 has a linear pressure scale. We obtained all PR-EoS fluid phase equilibrium modeling results using the computer program GPEC [25,26].

For the $CO_2 + n$-$C_{20}H_{42}$ system we obtained a single value for ΔV^{SL} by forcing the model to give a quadruple point (Q-point) at a temperature equal to the experimental Q-point temperature reported in Ref. [8]. Table 9 reports the only ΔV^{SL} value we used in this work for $CO_2 + n$-$C_{20}H_{42}$. It produces a SLL line (Fig. 7) less steep than the line that could be obtained directly from our experimental data (Fig. 2). Fig. 7 shows two SLV lines and a SLL line, all

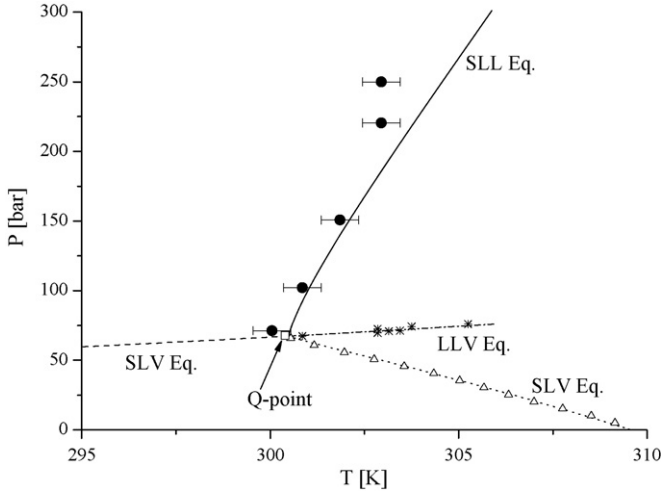

Fig. 7. *PT* projection of LLV, SLV and SLL equilibria for the system carbon dioxide + *n*-eicosane. Experimental data: (●) SLL equilibrium (this work); (△) SLV equilibrium (Huie et al. [8]); (*) LLV (this work); Q: quadruple point [8]. We also present the temperature experimental error bars for the SLL equilibrium. Lines: model. (—) SLL equilibrium; (- - -) SLV equilibrium (from quadruple point to low temperature); (···) SLV (from quadruple point to triple point of $C_{20}H_{42}$); (- · - · -) LLV equilibrium (from quadruple point to critical end point).

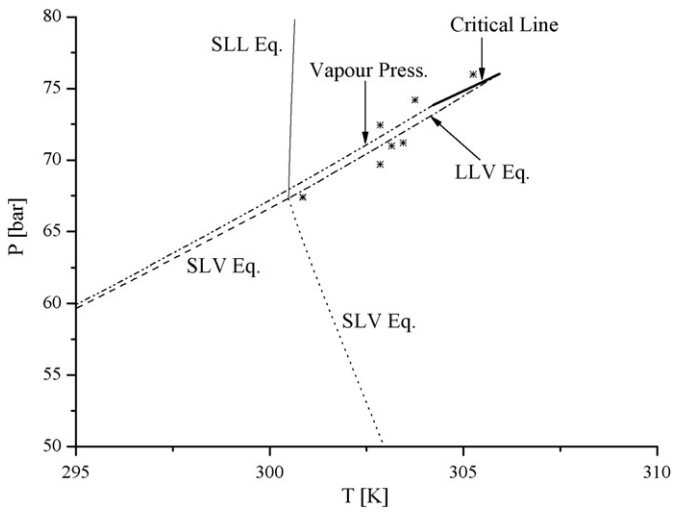

Fig. 8. *PT* projection for the system carbon dioxide + *n*-eicosane. (*) Experimental LLV equilibrium data (this work). Lines: model. (—) SLL equilibrium; (- - -) SLV equilibrium (from quadruple point to low temperature); (···) SLV (from quadruple point to triple point of $C_{20}H_{42}$); (- · - · -) LLV equilibrium (from quadruple point to critical end point); (- · · - · · -) vapor pressure of pure CO_2; (——) critical line (from CO_2 critical point, to critical end point).

of them calculated with the present model and parameters from Tables 6–9. It also shows our calculated LLV line. All four lines meet at the Q-point. Fig. 7 also presents our SLL and LLV experimental data together with the SLV experimental data of Huie et al. [8], which agree well with our model predictions. This is also the case for our LLV experimental data. Fig. 8 shows the same model results than Fig. 7, but in a narrower pressure range. It also presents the calculated vapor–liquid critical line and vapor–liquid saturation curve for pure CO_2. Notice that the CO_2 vapor pressure line and the LLV equilibrium lines are very close, as it was expected for this kind of systems [7]. Figs. 7 and 8 provide a fairly complete behavior map for the carbon dioxide + *n*-eicosane system at temperatures relatively close to the critical temperature of pure CO_2. Only one line, out of the four three-phase lines that meet at the Q point in Fig. 7, exists in a temperature range such that temperature is less that the Q temperature. This is similar to the case presented on page 56 of Ref. [3].

In Fig. 9 we present the temperature–composition projection that our model gives for the system carbon dioxide + *n*-eicosane, at conditions of three-phase equilibria, when one of the phases is solid *n*-eicosane. We label the phases at SLV equilibrium corresponding to the SLV line that extends from the quadruple point (Q) to the pure *n*-eicosane triple point as follows: V-LPHT (low-pressure/high-temperature vapor), L-LPHT (low-pressure/high-temperature liquid) and S (pure solid). For the phases at SLV equilibrium of the SLV line that stems from the quadruple point (Q) and extends towards lower temperatures, our labels are the following: V-LPLT (low-pressure/low-temperature vapor), L-LPLT (low-pressure/low-temperature liquid), and S (pure solid). For the SLL equilibrium line our labels are: L1 for the light liquid, L2 for the heavy liquid, and again S for the pure solid. Notice that the solid phases (S) are all located on the right end of Fig. 9, i.e., at a heavy component mole fraction equal to unity (pure compound). Fig. 9 indicates that at the Q-point the following transitions occur: vapor V-LPLT becomes vapor V-LPHT, liquid L-LPLT becomes liquid L1 and liquid L-LPHT becomes L2. On the other hand, lines V-LPHT, L-LPHT and S meet at the pure *n*-eicosane triple point. The maximum temperature in Fig. 9 (350 K) corresponds to 2400 bar approximately.

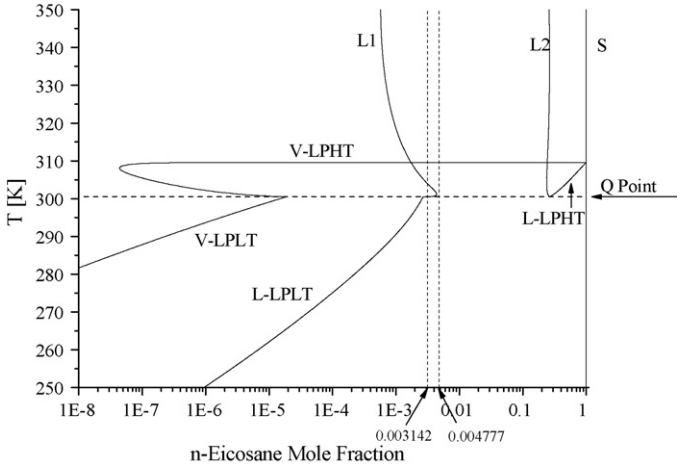

Fig. 9. Temperature–composition diagram for the system carbon dioxide + *n*-eicosane at conditions of three-phase equilibria. Lines: model. The phases at SLL equilibrium are: liquid 1 (L1), liquid 2 (L2) and pure solid (S). The phases at the SLV equilibrium that goes from the quadruple point (Q) to the *n*-eicosane triple point are: low-pressure/high-temperature vapor (V-LPHT), low-pressure/high-temperature liquid (L-LPHT), and pure solid (S). The three phases at the SLV equilibrium that starts at Q and goes to low temperature are: low-pressure/low-temperature vapor (V-LPLT), low-pressure/low-temperature liquid (L-LPLT), and pure solid (S). The vertical dashed lines correspond to isopleths discussed in Figs. 12 and 13.

Fig. 10 shows the pressure–composition projection of the SLL and SLV equilibria for the system carbon dioxide + *n*-eicosane. In this plot, as in Fig. 9, it is also possible to observe, at the quadruple point, the continuous nature of the liquid lines and of the vapor lines. It is clear too that the LPHT lines and the S line meet at a point having unity *n*-eicosane mole fraction. This point has a pressure value which corresponds to the triple point pressure that the heavy component has within the universe of the model (see Table 6).

Fig. 11 is similar to Fig. 10. The difference is in the nature (linear/log) of the scale for the mole fraction axis. Fig. 11 also includes the experimental data [8] for the liquid phase composition corresponding to the SLV line which develops between the quadruple point (Q) and the pure *n*-eicosane triple point. There is a good agreement here between the model and the experimental data.

Diagrams such as Fig. 9 are useful for calculating solid–fluid isopleths. Notice the vertical dashed line at 0.003142 $C_{20}H_{42}$ mole fraction. This line intersects twice the L1 phase of the SLL hyperline. Therefore, a pressure–temperature projection of the SL equilibrium isopleth at 0.003142 $C_{20}H_{42}$ mole fraction should intersect twice the *PT* projection of the SLL line. This is verified in Fig. 12 which presents for the system carbon dioxide + *n*-eicosane the calculated high-pressure segment of the Solid–fluid equilibrium isopleth at 0.003142 $C_{20}H_{42}$ mole fraction, together with the calculated three-phase equilibrium lines which we have included for reference. Fig. 12 also presents, for comparison, our experimental SLLE data and SLE data at 0.003142 $C_{20}H_{42}$ mole fraction. Fig. 9 also shows an intersection between the vertical dashed line at 0.003142 $C_{20}H_{42}$ mole fraction and the V-LPHT vapor. This means that there must exist, for the model, a solid–vapor segment for the 0.003142 $C_{20}H_{42}$ mole fraction isopleth, intersecting the low-pressure/high-temperature SLV line. We visualize such segment in Fig. 13 thanks to the log scale in the pressure axis. Notice that Fig. 13 presents mostly the same information than Fig. 12 plus our SLE experimental data at 0.00477 $C_{20}H_{42}$ mole fraction. Fig. 9 shows that at this last concentration value only the V-LPHT vapor line is intersected. Therefore, within the universe of the model, a solid–vapor segment exists for

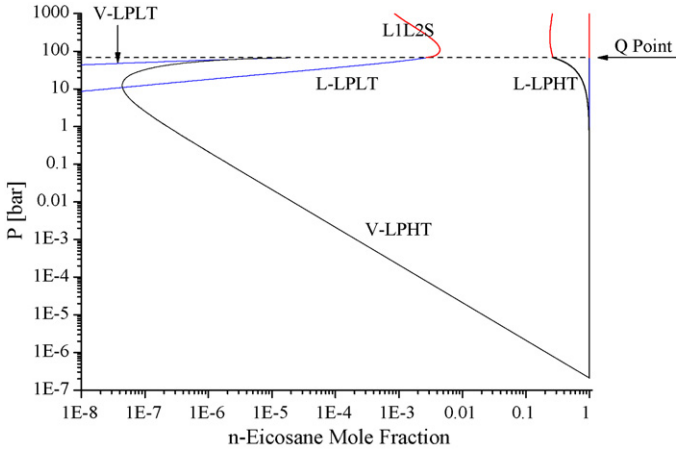

Fig. 10. Pressure–composition diagram for the system carbon dioxide + *n*-eicosane at conditions of three-phase equilibria. Lines: model (labels as in Fig. 9).

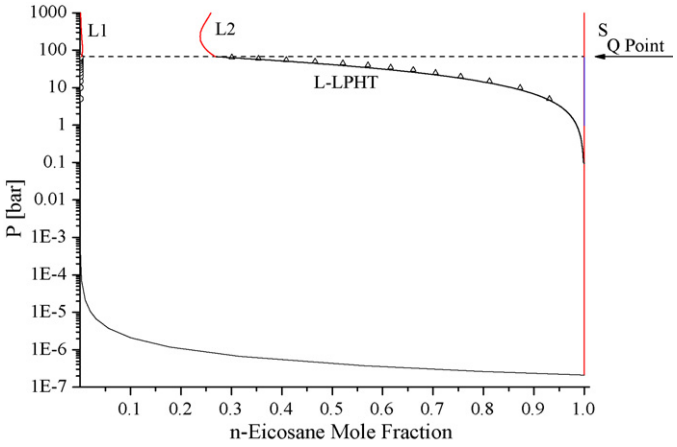

Fig. 11. Pressure–composition diagram of the system carbon dioxide + *n*-eicosane. This is similar to Fig. 10 but with a linear scale for the abscissa. This figure shows a comparison between the model (lines) and the experimental data (△) from Huie et al. [8], for the liquid phase at SLV equilibrium, for the SLV line which develops between the quadruple point (Q) and the *n*-eicosane triple point.

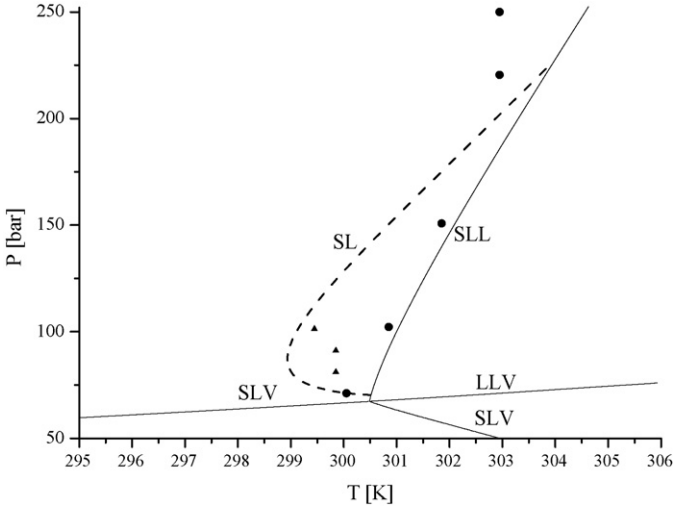

Fig. 12. Pressure–temperature diagram for the system carbon dioxide + *n*-eicosane. (- - -) Calculated high-pressure segment of the solid–fluid equilibrium isopleth at 0.003142 $C_{20}H_{42}$ mole fraction. The solid lines are the calculated three-phase equilibrium lines and have been included for reference. Experimental data (this work): (▲) SLE at 0.003142 $C_{20}H_{42}$ mole fraction; (●) SLLE. See in Fig. 9 the vertical line at 0.003142 $C_{20}H_{42}$ mole fraction.

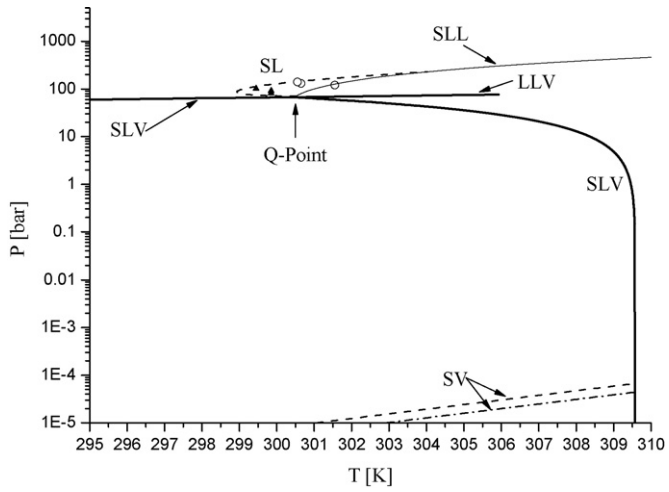

Fig. 13. Pressure–temperature diagram for the system carbon dioxide + *n*-eicosane. Calculated solid–vapor isopleths. (---) 0.003142 $C_{20}H_{42}$ mole fraction; (-·-·-) 0.004777 $C_{20}H_{42}$ mole fraction. The solid lines are the calculated three-phase equilibrium lines and have been included for reference. Experimental data (this work): (▲) SLE at 0.003142 $C_{20}H_{42}$ mole fraction; (◯) SLE at 0.004777 $C_{20}H_{42}$ mole fraction. See in Fig. 9 the vertical lines at 0.003142 and 0.004777 $C_{20}H_{42}$ mole fraction. The calculated high-pressure segment of the solid–fluid equilibrium isopleth at 0.003142 $C_{20}H_{42}$ mole fraction of Fig. 12 (---) is also shown here but this time using a logarithmic scale for pressure.

this isopleth (which we show in Fig. 13) but not a SL segment. This is in disagreement with our experimental SLE data. Notice, however, that the vertical dashed line at 0.00477 $C_{20}H_{42}$ mole fraction, is very close to the L1 line (Fig. 9). Thus, a slight change in the values of the model parameters should give the right qualitative behavior at 0.00477 $C_{20}H_{42}$ mole fraction. The reader should bear in mind that the only experimental information involving a solid phase that we considered to set the ΔV^{SL} value was the Q-point temperature for the system carbon dioxide + *n*-eicosane.

Fig. 13 shows only the solid–fluid segments of the 0.003142 $C_{20}H_{42}$ mole fraction isopleth. Fig. 14 completes such information by showing also the calculated fluid–fluid portions for such isopleth. The linear scale of the pressure axis makes the visualization of the solid–vapor segment impossible (such segment has already

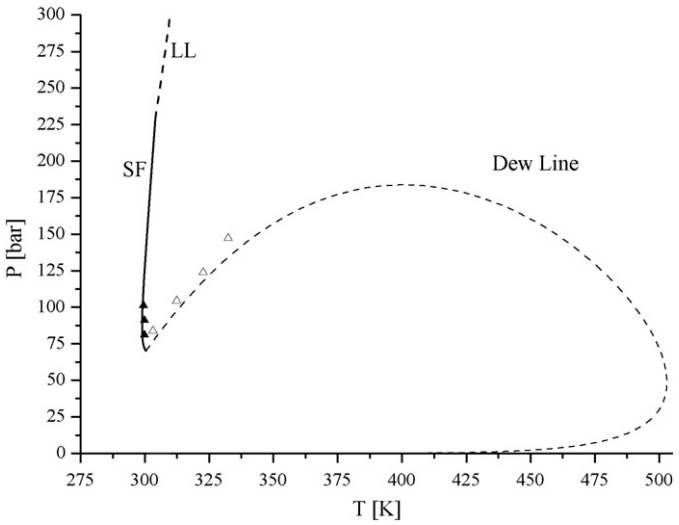

Fig. 14. Pressure–temperature projection of the isopleth at 0.003142 $C_{20}H_{42}$ fluid phase mole fraction for the system $CO_2 + C_{20}H_{42}$. Filled triangles: experimental solid–fluid equilibrium data (this work); empty triangles: experimental liquid–liquid equilibrium data (this work). Lines: model. (---) Dew line or liquid–liquid (LL) line; (—) solid–fluid equilibrium line (SF).

been shown in Fig. 13). Fig. 14 also presents our experimental SL and LL data for this isopleth. We observe, for the model, a dew line which has a continuous transition to a liquid–liquid line, which meets a SL line. This last line meets another LL line at higher pressure.

Notice that both, Figs. 6 and 14, show an acceptable agreement between the PR-EoS and the fluid–fluid equilibrium experimental data that we obtained in this work.

4. Summary, discussion and conclusions

In this work, we report phase equilibrium data that we measured for the asymmetric systems carbon dioxide + *n*-eicosane and propane + *n*-eicosane.

For the system carbon dioxide + *n*-eicosane, we obtained: [a] liquid–liquid (LL) equilibrium data (*T* range: 303.15–333.45 K, *P* range: 71.6–169.2 bar, liquid phase *n*-eicosane mole fraction (x_{C20}) range: from 0.001571 to 0.004777); [b] SL data (*T* range: 299.45–301.55 K, *P* range: 81.1–140.9 bar, liquid phase x_{C20} range: from 0.003142 to 0.004777); and [c] solid–liquid–liquid (SLL) equilibrium experimental data (*T* range: 300.05–302.95 K, *P* range: 71.2–250 bar). We also obtained some liquid–liquid–vapor (LLV) equilibrium experimental data for system carbon dioxide + *n*-eicosane (*T* range: 300.85–305.25 K, *P* range: 67.4–76 bar). We found a good agreement among our data and the SLV and LLV data from Huie et al. [8].

For the system propane + *n*-eicosane, we measured: [a] liquid–vapor (LV) isopleths in the temperature (*T*) range from 288.55 K to 333.45 K (pressure (*P*) range: from 8.4 to 21.9 bar, liquid phase *n*-eicosane mole fraction (x_{C20}) range: from 0.009816 to 0.747668), and, [b] solid–liquid (SL) transitions at constant composition (SL isopleths) in the *T* range from 287.05 K to 307.25 K (*P* range: 10.3–22.5 bar, liquid phase x_{C20} range: from 0.113130 to 0.747668). From such information we estimated the solid–liquid–vapor (SLV) locus, whose shape is the expected one.

We have also attempted to model the fluid phase equilibrium (FPE), the solid–fluid equilibrium (SFE) and the solid–fluid–fluid equilibrium (SFFE) for both systems. We used the Peng–Robinson Equation of State for the fluid phases and Eq. (1) for describing the fugacity of pure solid *n*-eicosane. The distinguishing feature of the present approach is the close attention to the reproduction of the pure heavy component solid–liquid equilibrium (melting) line [27,28].

With regard to the parameter values of the model, we first dealt with fluid–fluid equilibrium (FFE) and then with equilibria involving one or more fluid phases and a solid phase. We carried out the second step by searching for optimum values for variable ΔV^{SL}. This is the solid–liquid molar volume difference for the pure heavy component (*n*-eicosane). In the present approach, the pure heavy compound melting line is invariant with respect to the ΔV^{SL} value at set values of C_1, C_2 and C_3. ΔV^{SL} should have a unique value, since it should be a constant for *n*-eicosane. We have however found that we needed to use varying ΔV^{SL} values for correlating different isoplethic sets of SL data for the system propane + *n*-eicosane. On the other hand, for carbon dioxide + *n*-eicosane, a single value for ΔV^{SL} was enough to provide a quite acceptable performance for the model. However, the ΔV^{SL} value regressed from CO_2 + C20 data does not fall within the range of values corresponding to the system C3 + C20.

These limitations could be overcome in different ways. One possibility would be to fit all parameters simultaneously using the fluid–fluid and the solid–fluid experimental information together. Another possibility is to use more flexible mixing rules within the equation of state adopted for representing the fluid phases. We stress that what we have proposed in this work should be seen as a modeling approach, rather than as a specific model, for solid–fluid equilibria computations.

The model predicts a SLV locus with the proper shape for the system propane + *n*-eicosane. The model also describes properly the shapes of the SLL line and of the higher temperature SLV line of system CO_2 + C20. It also reproduces well the liquid phase composition at SLV equilibrium for the system CO_2 + C20. Therefore, we conclude that the model is basically able to grasp the complex observed behavior for the systems here studied. The richness of such behavior, which we obtained from coupling the Peng–Robinson (PR)-EoS with Eq. (1), may seem surprising to some readers, in view of the relative simplicity of Eq. (1) and of the PVTx relationship that defines de the PR-EoS. However, the simpler van der Waals (vdW) EoS already generates a wide variety of phase diagrams, as clearly shown by van Konynenburg and Scott, who "generated the first, nearly comprehensive classification of fluid phase equilibria" [29]. In other words, if a vdW-like EoS, such as the PR-EoS, can generate a widely varying behavior for fluid systems, then, the combination of such EoS with an equation for representing the fugacity of solids, e.g., Eq. (1), must produce a much greater number of patterns for the phase equilibria involving fluid and solid phases. However, such patterns may be difficult to obtain, due to the highly non-linear behavior of curves such as those in Fig. 9. The calculation methods of choice for tackling this problem are of the numerical continuation type [30], which are also named curve-tracking and/or path-following and/or tracing methods.

In situ wax formation can seriously hinder the process of recovering reservoir fluids (RFs). These are multicomponent mixtures with methane as the prevalent component. The presence of carbon dioxide, ethane and propane can also be considerable in RFs, e.g., in gas condensates and volatile oils [33]. Since carbon dioxide injection is used for enhanced oil recovery [34], the CO_2 concentration may become significantly greater than the natural RF CO_2 concentration. Thus, wax formation in (multicomponent) reservoir fluids can be influenced, among other components, by propane and carbon dioxide. The experimental data obtained in this work contribute to the knowledge of the macroscopic manifestations of the interactions between propane or carbon dioxide and the wax-like component eicosane, under fluid–fluid and solid–fluid equilibrium conditions. Such binary data can be used to fit parameters for models developed to describe the multicomponent equilibria found in reservoir fluids. This is because conventional models typically rely on binary parameters for predicting the properties of multicomponent systems. Besides, the experimental data obtained in the present work could also be helpful in the development of models to be used in the simulation of supercritical synthetic-wax fractionation processes [35]. Progress in the modeling of the phase equilibria of multicomponent asymmetric systems requires a good understanding of the behavior of models over wide ranges of conditions for binary systems. This can be achieved by the application of systematic methods for generating both, binary global phase equilibrium diagrams involving fluid and solid phases, and, subsequently, binary phase diagrams at constant temperature/pressure/composition. This is the approach we used in this work, and the one we recommend to readers interested in studying the properties of complex highly asymmetric mixtures.

Acknowledgements

We gratefully acknowledge the financial support by the Argentinean institutions Consejo Nacional de Investigaciones Científicas y Técnicas de la República Argentina (CONICET), Universidad Nacional del Sur (U.N.S.), Universidad Nacional de Córdoba (U.N.C.) and Agencia Nacional de Promoción Científica y Tecnológica (ANPCyT), and by CNPq (Brasil).

Appendix A. Estimation of uncertainty levels for experimental concentrations of carbon dioxide, propane and *n*-eicosane

The weight fractions ($w_{C_{20}H_{42}}$ and w_{light}), and mole fractions ($x_{C_{20}H_{42}}$ and x_{light}), of the heavy ($C_{20}H_{42}$) and light (CO_2 or C_3H_8) components are given by the following equations:

$$w_{C_{20}H_{42}} = \frac{m_{C_{20}H_{42}}}{m_{C_{20}H_{42}} + m_{light}} \tag{A.1}$$

$$w_{light} = \frac{m_{light}}{m_{C_{20}H_{42}} + m_{light}} \tag{A.2}$$

$$x_{C_{20}H_{42}} = \frac{m_{C_{20}H_{42}}/MW_{C_{20}H_{42}}}{(m_{C_{20}H_{42}}/MW_{C_{20}H_{42}}) + (m_{light}/MW_{light})} \tag{A.3}$$

$$x_{light} = \frac{m_{light}/MW_{light}}{(m_{C_{20}H_{42}}/MW_{C_{20}H_{42}}) + (m_{light}/MW_{light})} \tag{A.4}$$

In the above equations $m_{C_{20}H_{42}}$ and m_{light} are, respectively, the masses of *n*-eicosane and light component (CO_2 or C_3H_8) loaded into de equilibrium cell, while $MW_{C_{20}H_{42}}$ and MW_{light} stand for the corresponding molecular masses. The mass of $C_{20}H_{42}$ ($m_{C_{20}H_{42}}$) is directly measured by using a precision balance, with an estimated uncertainty of ±0.0001 g ($\lambda_{m_{C_{20}H_{42}}} = 0.0001$ g). The mass of the light compound (CO_2 or C_3H_8) loaded into the cell is calculated from the following equation:

$$m_{light} = \rho_{light}(V^0_{light} - V^F_{light}) \tag{A.5}$$

In Eq. (A.5) V^0_{light} is the total volume of light component stored within the syringe pump [under controlled temperature (T_{pump}) and pressure (P_{pump}) conditions] before loading the cell with such component. On the other hand, V^F_{light} is the total volume of light component remaining in the syringe pump, after completion of the light component loading process. The temperature and pressure conditions at which V^F_{light} is measured are the same than for V^0_{light}. In this work, T_{pump} and P_{pump} were 280.15 K and 150 bar, for Carbon dioxide, and 278.15 K and 50 bar for propane. The uncertainty in the measured values of T_{pump} and P_{pump} were estimated to be ±0.5 K ($\lambda_{T_{pump}} = 0.5$ K) and ±2.59 bar ($\lambda_{P_{pump}} = 2.59$ bar), respectively. ρ_{light} is the density of the light component at T_{pump} and P_{pump}. T_{pump} and P_{pump} have values that guarantee a single phase for the light component stored in the syringe pump. For both pure compounds, we obtained ρ_{light} from the NIST Chemistry WebBook [31]. The experimental uncertainty in V^0_{light} and/or V^F_{light} is estimated to be ±0.01 ml ($\lambda_{V^0_{light}} = \lambda_{V^F_{light}} = 0.01$ ml). From Eqs. (A.1) to (A.5), it is clear that the variables $w_{C_{20}H_{42}}$, w_{light}, $x_{C_{20}H_{42}}$ and x_{light} are functions of the (directly measured) independent variables $m_{C_{20}H_{42}}$, V^0_{light}, V^F_{light}, T_{pump} and P_{pump}. From standard propagation of error analysis [32], we write:

$$\lambda_{z_i} = \left|\frac{\partial z_i}{\partial m_{C_{20}H_{42}}}\right| \lambda_{m_{C_{20}H_{42}}} + \left|\frac{\partial z_i}{\partial V^0_{light}}\right| \lambda_{V^0_{light}} + \left|\frac{\partial z_i}{\partial V^F_{light}}\right| \lambda_{V^F_{light}} + \left|\frac{\partial z_i}{\partial T_{pump}}\right| \lambda_{T_{pump}} + \left|\frac{\partial z_i}{\partial P_{pump}}\right| \lambda_{P_{pump}} \tag{A.6}$$

In Eq. (A.6) λ_{z_i} is the estimated uncertainty in the dependent variable z_i, which represents any of the variables $w_{C_{20}H_{42}}$, w_{light}, $x_{C_{20}H_{42}}$ and x_{light}. Symbols $\lambda_{m_{C_{20}H_{42}}}$, $\lambda_{V^0_{light}}$, $\lambda_{V^F_{light}}$, $\lambda_{T_{pump}}$ and $\lambda_{P_{pump}}$ represent the estimated uncertainties in the independent variables. The partial derivatives in Eq. (A.6) are obtained analytically for the case of the first three terms of the right hand side of Eq. (A.6). The

derivatives with respect to T_{pump} and P_{pump} are computed as follows:

$$\frac{\partial z_i}{\partial T_{pump}} = \frac{\partial z_i}{\partial m_{light}} \frac{\partial m_{light}}{\partial T_{pump}} = \frac{\partial z_i}{\partial m_{light}} \left[(V^0_{light} - V^F_{light}) \frac{\partial \rho_{light}}{\partial T_{pump}} \right] \quad \text{(A.7)}$$

$$\frac{\partial z_i}{\partial P_{pump}} = \frac{\partial z_i}{\partial m_{light}} \frac{\partial m_{light}}{\partial P_{pump}} = \frac{\partial z_i}{\partial m_{light}} \left[(V^0_{light} - V^F_{light}) \frac{\partial \rho_{light}}{\partial P_{pump}} \right] \quad \text{(A.8)}$$

The partial derivative $\partial z_i/\partial m_{light}$ is obtained analytically. On the other hand, the partial derivatives $\partial \rho_{light}/\partial T_{pump}$ and $\partial \rho_{light}/\partial P_{pump}$ are computed numerically from information on densities for CO_2 (or for C_3H_8) in narrow enough ranges of temperature and pressure, centered at the point (T_{pump}, P_{pump}). We obtained density values for CO_2 and/or C_3H_8 from the NIST Chemistry WebBook [31]. The values we used for the estimated uncertainties of the directly measured variables are $\lambda_{m_{C_{20}H_{42}}} = 0.0001$ g, $\lambda_{V^0_{light}} = 0.01$ ml, $\lambda_{V^F_{light}} = 0.01$ ml, $\lambda_{T_{pump}} = 0.5$ K and $\lambda_{P_{pump}} = 2.59$ bar. Notice that λ_{z_i} is an absolute uncertainty. The relative percent uncertainty is calculated as $(100\lambda_{z_i}/z_i)$. Although we computed the percent uncertainty in $w_{C_{20}H_{42}}$, w_{light}, $x_{C_{20}H_{42}}$ and x_{light} for every experimental point, we only report, in the main text, the maximum and average values. Finally, notice that in the present propagation of error analysis we have assumed that the uncertainties in the molecular masses of the components have negligible effects on the uncertainties of variables $w_{C_{20}H_{42}}$, w_{light}, $x_{C_{20}H_{42}}$ and x_{light}.

References

[1] M. Christov, R. Dohrn, High-pressure fluid phase equilibria. Experimental methods and systems investigated (1994–1999), Fluid Phase Equilibr. 202 (2002) 153–218.

[2] J.R. Elliott, C.T. Lira, Introductory Chemical Engineering Thermodynamics, Prentice-Hall PTR, Upper Saddle River, NJ, ISBN (0-13-011386-7), 1999, pp. 445–458.

[3] R. Koningsveld, W.H. Stockmayer, E. Nies, Polymer Phase Diagrams, Oxford University Press, Oxford, NY, 2001.

[4] J. Gregorowicz, Th.W. de Loos, J. de Swaan Arons, The system propane + eicosane: *P*, *T*, and *x* measurements in the temperature range 288–358 K, J. Chem. Eng. Data 37 (1992) 356–358.

[5] R.L. Scott, P.H. van Konynemburg, Part 2. Static properties of solutions. Van der Waals and related models for hydrocarbon mixtures, Discuss. Faraday Soc. 49 (1970) 87–97.

[6] C.J. Peters, H.J. van der Kooi, J.L. de Roo, J. de Swaan Arons, J.S. Gallagher, J.M.M. Levelt Sengers, The search for tricriticality in binary mixtures of near-critical propane and normal paraffins, Fluid Phase Equilibr. 51 (1989) 339–351.

[7] K.D. Luks, The occurrence and measurement of multiphase equilibria behavior, Fluid Phase Equilibr. 29 (1986) 209–224.

[8] N.C. Huie, K.D. Luks, J.P. Kohn, Phase-equilibria behavior of systems carbon dioxide-*n*-eicosane and carbon dioxide-*n*-decane-*n*-eicosane, J. Chem. Eng. Data 18 (3) (1973) 311–313.

[9] K.A.M. Gasem, R.L. Robinson Jr., Solubilities of carbon dioxide in heavy normal paraffins (C20–C44) at pressures to 9.6 MPa and temperatures from 323 to 423 K, J. Chem. Eng. Data 30 (1) (1985) 53–56.

[10] S.H. Huang, H.M. Lin, K.C. Chao, Solubility of carbon dioxide, methane, and ethane in *n*-eicosane, J. Chem. Eng. Data 33 (2) (1988) 145–147.

[11] A. Kordikowski, G.M. Schneider, Fluid phase equilibria of binary and ternary mixtures of supercritical carbon dioxide with low-volatility organic substances up to 100 MPa and 393 K: cosolvency effects and miscibility windows, Fluid Phase Equilibr. 90 (1993) 149–162.

[12] Y. Sato, Y. Tagashira, D. Maruyama, S. Takishima, H. Masuoka, Solubility of carbon dioxide in eicosane, docosane, tetracosane, and octacosane at temperatures from 323 to 473 K and pressures up to 40 MPa, Fluid Phase Equilibr. 147 (1998) 181–193.

[13] I. Nieuwoudt, M. du Rand, Measurement of phase equilibria of supercritical carbon dioxide and paraffins, J. Supercrit. Fluids 22 (2002) 185–199.

[14] M. Cismondi, M.L. Michelsen, Global phase equilibrium calculations: critical lines, critical end points and liquid–liquid-vapour equilibrium in binary mixtures, J. Supercrit. Fluids 39 (2007) 287–295.

[15] P.M. Ndiaye, E. Franceschi, D. Oliveira, C. Dariva, F.W. Tavares, J.V. Oliveira, Phase behavior of soybean oil, castor oil and their fatty acid ethyl esters in carbon dioxide at high pressures, J. Supercrit. Fluids 37 (2006) 29–37.

[16] E. Franceschi, M.B. Grings, C.D. Frizzo, J.V. Oliveira, C. Dariva, Phase behavior of lemon and bergamot peel oils in supercritical CO_2, Fluid Phase Equilibr. 226 (2004) 1–8.

[17] M.L. Corazza, L. Cardozo Filho, O.A.C. Antunes, C. Dariva, Phase behavior of the reaction medium of limonene oxidation in supercritical carbon dioxide, Ind. Eng. Chem. Res. 42 (2003) 3150–3155.

[18] P.L. Cheong, D. Zhang, K. Ohgaki, B.C.-Y. Lu, High pressure phase equilibria for binary systems involving a solid phase, Fluid Phase Equilibr. 29 (1986) 555–562.

[19] D.J. Fall, J.L. Fall, K.D. Luks, Liquid–liquid–vapor immiscibility limits in carbon dioxide + *n*-paraffin mixtures, J. Chem. Eng. Data 30 (1985) 82–88.

[20] H.J. van der Kooi, E. Flöter, Th.W. de Loos, High-pressure phase equilibria of $\{(1-x)CH_4 + xCH_3(CH_2)_{18}CH_3\}$, J. Chem. Thermodyn. 27 (1995) 847.

[21] D.Y. Peng, D.B. Robinson, A new two-constant equation of state, Ind. Eng. Chem. Fundam. 15 (1976) 59–64.

[22] DIPPR 801, Evaluated Process Design Data, Public Release (2003), American Institute of Chemical Engineers, Design Institute for Physical Property Data, BYU-DIPPR, Thermophysical Properties Laboratory. Provo, Utah.

[23] A. Firoozabadi, Thermodynamics of Hydrocarbon Reservoirs, 1st ed., McGraw-Hill, 1999 (Chapter 5).

[24] SPECS V5.24 – IVC-SEP, Institut for Kemiteknik, Danmarks Tekniske Universitet, Lyngby, DENMARK, www.ivc-sep.kt.dtu.dk.

[25] M. Cismondi, D.N. Nuñez, M.S. Zabaloy, E.A. Brignole, M.L. Michelsen, J.M. Mollerup, GPEC: A Program for Global Phase Equilibrium Calculations in Binary Systems. EQUIFASE 2006: VII Conferencia Iberoamericana sobre Equilibrio entre Fases para el Diseño de Procesos, Morelia, Michoacán, México, October 21–25, 2006. Full paper available in EQUIFASE 2006 CD-ROM.

[26] M. Cismondi, M.L. Michelsen, M.S. Zabaloy, Automated generation of phase diagrams for supercritical fluids from equations of state, in: 11th European Meeting on Supercritical Fluids, Barcelona-Spain, May 4–7, 2008.

[27] S.B. Rodriguez-Reartes, M. Cismondi, M.S. Zabaloy, Numerical continuation method for high pressure solid–fluid equilibrium calculations in asymmetric systems, in: 23rd European Symposium on Applied Thermodynamics, Cannes-France, May 29–June 1, 2008. Work (PII-57).

[28] S.B. Rodriguez-Reartes, M. Cismondi, M.S. Zabaloy. High pressure solid–fluid equilibrium in asymmetric systems. I Iberoamerican Conference of Supercritical Fluids-PROSCIBA (2007), Iguassu Falls, April 10–13, 2007. Full paper available in PROSCIBA 2007 CD-ROM (SC-048).

[29] J. de Swaan Arons, Th.W. de Loos, Phase behavior: phenomena, significance, and models, in: S.I. Sandler (Ed.), Models for Thermodynamic and Phase Equilibria Calculations, Marcel-Dekker, New York, 1993, p. 442.

[30] E.L. Allgower, K. Georg, Numerical path following, in: P.G. Ciarlet, J.L. Lions (Eds.), Handbook of Numerical Analysis, vol. 5, North-Holland, 1997, pp. 3–207.

[31] E.W. Lemmon, M.O. McLinden, D.G. Friend, Thermophysical properties of fluid systems, in: P.J. Linstrom, W.G. Mallard (Eds.), NIST Chemistry WebBook, NIST Standard Reference Database Number 69, National Institute of Standards and Technology, Gaithersburg, MD 20899, http:webbook.nist.gov (retrieved May 14, 2009).

[32] D.P. Shoemaker, C.W. Garland, Experiments in Physical Chemistry, McGraw-Hill Book Company, NY, 1967, p. 30.

[33] K.S. Pedersen, Aa. Fredenslund, P. Thomassen, Properties of Oils and Natural Gases, Gulf Publishing Company, Houston, 1989, p. 7.

[34] Y.-F. Hu, S. Li, Y.-P. Chu, T.-M. Guo, Wax precipitation in three Chinese reservoir oils under carbon dioxide (CO_2) injection, Energy Fuels 18 (2004) 1183–1186.

[35] C.E. Schwarz, I. Nieuwoudt, Phase equilibrium of propane and alkanes. Part I. Experimental procedures, dotriacontane equilibrium and EoS modeling, J. Supercrit. Fluids 27 (2) (2003) 133–144.